Electronic structure of representative band-gap materials by all-electron quasiparticle self-consistent *GW* calculations

Nora Salas-Illanes,* Dmitrii Nabok, and Claudia Draxl†

Physics Department and IRIS Adlershof, Humboldt-Universität zu Berlin, Zum Großen Windkanal 2, 12489 Berlin, Germany and European Theoretical Spectroscopic Facility (ETSF)

(Received 12 November 2021; revised 13 July 2022; accepted 14 July 2022; published 27 July 2022)

In this work, we report results of the quasiparticle self-consistent *GW* method within the framework of the linearized augmented plane-wave method. The impact of self-consistency on the electronic structure is investigated with the examples of nine semiconductors and insulators, namely, Ar, Si, SiC, C, BN, LiF, MgO, CaO, and GaAs. Possible reasons for discrepancies between different studies and implementations are discussed. For LiF, MgO, and CaO, we assess the charge-density redistribution upon self-consistency. For a representative set of materials, we investigate and confirm the absence of (any) starting-point dependence. The off-diagonal terms in the self-energy matrix are found to considerably impact the electronic structure. For better reproducibility and quality assessment, we describe the implementation of QSGW in the all-electron full-potential code EXCITING.

DOI: 10.1103/PhysRevB.106.045143

I. INTRODUCTION

Tailoring materials for any application requires a thorough understanding of their electronic structure. In the past decades, density functional theory [1] (DFT) has been the most popular numerical method to calculate properties of many-electron systems in the ground state (GS). Indeed, for a large number of materials, DFT provides accurate results for properties derived from the ground-state energy. In practice, DFT is implemented in terms of the Kohn-Sham (KS) scheme [2]. In this scheme, the electron-electron interaction is approximated by a mean-field exchange-correlation potential v_{xc}. Since KS particles represent a fictitious, auxiliary system, their eigenvalues do not reflect real one-electron energies but a first approximation in terms of the independent-particle (IP) picture. Nevertheless, even if falling short of describing excited states, the KS band structure gives a first insight in the electronic structure of the system.

In order to access one-electron energies for addressing excited states, one can use many-body perturbation theory (MBPT), where electrons are described as *quasiparticles* (QP). Quasielectrons are "dressed" with their interaction with all other electrons. The QP acquires an energy, called *self-energy* $\Sigma(\omega)$, that arises from the perturbation the QP causes in the system. Within MBPT, we express this dynamical quantity through the *GW* approximation (GWA) [3].

Central to the GWA, the Green's function G provides the propagation of the QP upon its removal from or addition to the system in the GS [4]. Unfortunately, G is a complicated object defined by the unknown eigenstates of the interacting QP. In practice, G can be approximated to a single-particle, noninteracting Greens's function G_0, usually built from DFT eigenfunctions. This operator, together with the screened Coulomb interaction in the random phase approximation (RPA), W_0, provides the lowest-order approximation to the self-energy Σ. Treating the difference between Σ and V_{xc} in first-order perturbation theory provides corrections to the KS eigenvalues. This approach is known as one-shot *GW* [5] or G_0W_0. Although often successful when calculating band gaps, the G_0W_0 approximation builds upon KS results and therefore depends on the energies and eigenstates provided by the chosen v_{xc}. This phenomenon is known as *starting-point dependence* [6,7]. Possible solutions to this starting-point dependence are self-consistent schemes [8–11]. Here we focus on the *quasiparticle self-consistent GW* (QSGW) method [12–14]. Within this framework, one arrives at the interacting G through the iterative optimization of v_{xc}. In other words, in every step of the cycle, G_0 is updated, finally converging to the solution closest to G. We have implemented the QSGW method into the all-electron full-potential code EXCITING that makes use of linearized augmented plane-wave (LAPW) basis functions to describe the one-electron states and a mixed-product basis [15–17] to represent nonlocal operators in *GW* and hybrid-functional calculations.

We start with a summary of the QSGW method. Our results comprise electronic properties of nine semiconductors and insulators, covering details of the band structures and examples of charge densities. We then assess the starting-point dependence and provide insight in the role of off-diagonal terms of the self-energy. In the Implementations section, we briefly describe the basis sets for GS and excited-states calculations followed by specific aspects of the implementation of QSGW in EXCITING. Since different approximations, algorithms, and computational parameters introduced in different codes and calculations may give rise to significant discrepancies, detailed information is inevitable in view of reproducibility of calculations. For this reason, we also point to the input and output files of our calculations available in the NOMAD

*nora.illanes@physik.hu-berlin.de
†claudia.draxl@physik.hu-berlin.de

Repository [18]. The used computational parameters and their impact on the results are provided in the Appendix.

II. METHODOLOGY

Following Fermi-liquid theory, there is a one-to-one correspondence between a bare and dressed particle, i.e., QP. *GW*, being a realization of MBPT, regards interacting fermions as dressed particles. In *fully self-consistent GW* (scGW), the Green function G is updated by the self-consistent solution of the Dyson equation, starting from an initial guess for the self-energy.

QSGW is an alternative self-consistent method within the realm of GWA, suggested by Kotani, Schilfgaarde, and Faleev [12–14]. It considers conservation laws and provides a practical recipe to build the iterative procedure. It can be best understood through the adiabatic connection of a bare particle to a dressed one. The difference between these two is the interaction potential, where their one-to-one correspondence allows the independent-particle system to evolve into the fully interacting one. Here, the Kohn-Sham particles [called independent particles (IP) in the following] serve as a zeroth approximation to the bare particles, i.e., as the starting point of QSGW.[1]

The Kohn-Sham particles interact through an effective potential v_{eff} that comprises the lattice and Hartree potentials V and v_H, respectively, and the exchange-correlation potential v_{xc}. The initial, independent-particle Hamiltonian H_0 is made up by v_{eff} and the kinetic energy T. In general terms, the effective potential in H_0 can include any static, local, or nonlocal v_{xc}. In QSGW, H is split into H_0 and a residual part $H_0 - H$. This last contribution is small and thus considered as a perturbation, leaving the momentum of the bare QP unaffected. This residual part is minimized by finding an *optimal* effective potential $v_{\text{xc}}^{\text{opt}}$. In that way, the QSGW method searches for the "best" possible candidate for G_0, i.e., the one closest to the interacting G. To carry out this optimization, $v_{\text{xc}}^{\text{opt}}$ is determined self-consistently [14]. Finally, the converged potential $v_{\text{xc}}^{\text{opt}}$ replaces the initial v_{xc} in the independent-particle Hamiltonian H_0.

The potential $v_{\text{xc}}^{\text{opt}}$ is calculated as

$$v_{\text{xc}}^{\text{opt}} = \frac{1}{2}\sum_{nl} |\psi_n\rangle \{ \text{Re}[\Sigma_{xc}(\epsilon_n)]_{nl} + \text{Re}[\Sigma_{xc}(\epsilon_l)]_{nl} \} \langle\psi_l|, \quad (1)$$

with n, l being band indices and $[\dots]_{nl}$ indicating the corresponding matrix elements. For simplicity, we have left out the **k** dependence in this expression. Here only the real part of the self-energy is considered.

Kotani and coworkers derived the optimal effective potential through a norm-functional formalism. The potential $v_{\text{opt}}^{\text{xc}}$ guarantees that the energy functional $F[G]$ reaches its lowest value upon variation [19–21]. The measure defining the lowest value is the squared length of the functional derivative $||D(\omega)||^2$. Taking the Klein functional as reference, Ismail-Beigi has proven [21] that F is independent of variations of v_{eff} or, equivalently, of the starting point G_0. On the other hand, varying G with a fixed G_0, implies a variation in F:

$$\delta F|_{G_0} = \int_{-\infty}^{\infty} \frac{d\omega}{2\pi i} e^{i\omega 0^+} \text{tr}\big\{ -G_0^{-1}(\omega)\delta G(\omega) + G^{-1}(\omega)\delta G(\omega) - (v_H - v_{\text{xc}})\delta G(\omega)\big\} + \delta E_H[\rho] + \delta\Phi_{\text{xc}}[G]. \quad (2)$$

The variation of the Hartree energy E_H with respect to to G is equal to $v_H\delta G$, canceled out by the third term in the trace, and the variation of the Luttinger-Ward functional $\delta\Phi_{\text{xc}}[G]$ can be written as $\Sigma_{\text{xc}}\delta G$. Factorizing δG out, the trace reads as $[G^{-1} - G_0^{-1} + \Sigma_{\text{xc}} - v_{\text{xc}}]\delta G$. To replace δG, we use the Dyson equation with fixed G_0 and parametrize G by a trial self-energy Σ_t:

$$G^{-1} = \omega I - T - V - v_H - \Sigma_t = G_0^{-1} - [\Sigma_t - v_{\text{xc}}], \quad (3)$$

$$\delta G = G\,\delta\,\Sigma_t\,G. \quad (4)$$

Note that in order to arrive at Eq. (2), the relation $\delta\,\text{tr}\{\ln(A)\} = \text{tr}\{A^{-1}\delta A\}$ has been used to rewrite the Klein functional, and for the derivation of G above one makes use of the variation of an inverse, i.e., $\delta[A^{-1}] = -A^{-1}[\delta A]A^{-1}$, and the cyclicity of the trace $\text{tr}\{ABC\} = \text{tr}\{BCA\}$ has been employed for the matrix derivative in Eq. (5). The variation of the functional with respect to the trial potential finally reads as (without explicitly indicating the frequency dependence)

$$2\pi i\frac{\delta F}{\delta\Sigma_t} = G\big[G^{-1} - G_0^{-1} + \Sigma_{\text{xc}} - v_{\text{xc}}\big]G. \quad (5)$$

To facilitate the search, it is reasonable to delimit the search space for all possible G to all possible G_0 of the system because G_0 is already connected to a physically grounded Hamiltonian. Doing so, i.e., replacing G_0 in Eq. (5), the expression becomes

$$2\pi i\frac{\delta F}{\delta\Sigma_t} = G_0[\Sigma_{\text{xc}} - v_{\text{xc}}]G_0. \quad (6)$$

$||D_0||^2$ is the square of the length of the matrix in Eq. (6) in the basis of $|n\rangle$, in which G_0 is diagonal in the Lehman representation:

$$||D_0(\omega)||^2 = \int_{-\infty}^{\infty}\sum_{nl}\frac{|\langle n|\Sigma_{\text{xc}}(\omega) - v_{\text{xc}}|l\rangle|^2}{[(\omega-\epsilon_n)+\eta^2][(\omega-\epsilon_l)+\eta^2]}, \quad (7)$$

where η is a small positive quantity representing the decay rate of the state with energy ϵ_n [19]. When minimizing the integral in Eq. (7), one needs to distinguish between diagonal and off-diagonal terms. The former show a leading contribution, scaling as η^{-3}, which turns to zero if $\langle n|\text{Re}[\Sigma_{\text{xc}}(\epsilon_n)]|n\rangle = \langle n|v_{\text{xc}}|n\rangle$. In the off-diagonal terms, the largest contribution, scaling as η^{-1}, comes from the poles $\epsilon_n + i\eta$ and $\epsilon_l + i\eta$. Finally, Eq. (1) follows from the minimization of the latter, as explained in detail in Ref. [20].

Solving the secular equation for H_0 with the newly derived optimized potential returns new energies and eigenvectors. One then solves Hedin's equations and updates again $v_{\text{xc}}^{\text{opt}}$,

[1]They are termed bare QPs in Ref. [14].

TABLE I. Energy gaps E_Δ (eV) at Γ and between Γ (VBM) and X (in most cases CBM) as obtained for the *production settings* (see Table VI). Corrections for fully converged results of selected materials are provided in Appendix C, Table VIII. For Si and C, the fundamental band gap E_g is indirect with the CBM not at a high-symmetry point. In the last row, the experimental values are corrected for zero-point renormalization and spin-orbit coupling (SOC), unless noted by a subscript e. If more than one reference is provided, the first one refers to the experimental gap, while the other one to the correction(s). In case of GaAS, the third one points to the SOC.

E_Δ/eV		SiC	Si	BN	MgO	CaO	LiF	Ar	C	GaAs
QSGW	Γ-Γ	8.35	3.64	12.61	9.97	8.68	17.09	15.34	8.41	2.24
	Γ-X	3.00	1.59	7.62	14.25	8.06	23.48	18.12	7.01	2.32
	E_g	3.00	1.39	7.62	9.97	8.06	17.09	15.34	6.23	2.24
G_0W_0	Γ-Γ	7.47	3.18	11.18	7.46	6.54	13.86	12.99	7.33	1.28
	Γ-X	2.35	1.17	6.30	11.79	6.01	20.07	15.84	5.95	1.83
LDA	Γ-Γ	6.42	2.52	8.68	4.62	4.56	8.94	8.18	5.54	0.27
	Γ-X	1.29	0.60	4.35	8.91	3.48	14.55	10.85	4.41	1.34
Expt.	E_g	2.50	1.23	6.66	7.98	7.1_e	14.48	14.20_e	5.89	1.69
Refs.		[34,35]	[35,36]	[37,38]	[38,39]	[39]	[38,40]	[31]	[34,35]	[14,36,41]

repeating this cycle until self-consistency. This way, the single-electron state $\psi_{n\mathbf{k}}$ has become the quasiparticle wave function $\psi^{\mathrm{QP}}_{n\mathbf{k}}$ with associated eigenvalue $\epsilon^{\mathrm{QP}}_{n\mathbf{k}}$.

We note in passing that QSGW inherits the main approximation of GWA, namely, neglecting vertex corrections. This impacts the final results due to the omitted electron-hole interactions, e.g., leading to underestimated dielectric screening, that is reflected in overestimated band gaps [22]. To address this issue, possible corrections to QSGW have been suggested in literature [23,24]. Aside from this approximation, the optimized potential is static, i.e., the full energy dependence of the self-energy is dropped. Also, Hermiticity is forced by neglecting the imaginary part of the self-energy in its evaluation. The latter, nevertheless, can be computed, providing the inverse of the QP's lifetime.

III. RESULTS

The selected cubic bulk semiconductors and insulators are listed in Table VI in Appendix B. In general, the respective IP calculations are performed with the local-density approximation (LDA), unless when probing the starting-point dependence. Like in previous works [25,26] for interpolating the electronic structure from G_0W_0 and QSGW results onto a denser $\mathbf{q}$ grid, we use maximally localized Wannier functions [27–29]. This scheme has been implemented in EXCITING recently [30]. Computational parameters and details can be found in the Appendices.

A. Quasiparticle electronic structure

For any of the here investigated material, the valence band region obtained by LDA, G_0W_0, and QSGW exhibits the same overall features, albeit shifted energies. With no exception, the valence band maximum (VBM) in QSGW is shifted downwards in energy with respect to G_0W_0 and LDA, while the opposite is true for the conduction band minimum (CBM). Assessing the impact of self-consistency along the X-Γ direction, i.e., the region of the direct and indirect band gaps (Table I), we neither see a rigid shift relative to G_0W_0 nor to LDA. In other words, aside from changed band gaps, the bands exhibit slightly different dispersion and, hence, band masses. Only for MgO (see Fig. 1) the changes relative to LDA are the same, for both QSGW and G_0W_0 results. Overall, we observe, that the G_0W_0 values in Table I are in many instances closer to the experimental values than those calculated with QSGW.

Overestimation of fundamental band gaps by the QSGW method is known from the literature [14,31,32]. Overall, we confirm this. As an example, looking at absolute energies, the values obtained from our calculations for SiC and GaAs deviate by ≈ 0.5 eV with respect to experiment, corresponding to +19% and +33%, respectively. Another option is to correlate this finding with the impact when starting from a semilocal functional. For instance, we find the largest increase in the band gaps of Ar, changing from 8.18 to 15.34 (7.16-eV increase) compared to LDA and LiF (8.16-eV increase, from 8.94 to 17.10). The distinct amounts of discrepancies of 1.13 and 2.62 eV relative to the experimental counterparts, respectively, suggest that there is no direct correlation. However, we cannot draw a final conclusion without considering the starting-point dependence of G_0W_0 results which is thoroughly discussed in the literature [13,32,33]. Moreover, there are also other sources for discrepancies to be taken into account, which are discussed at the end of this section.

The differences in band energies between QSGW and the other methods also show up at low-energy states. As an

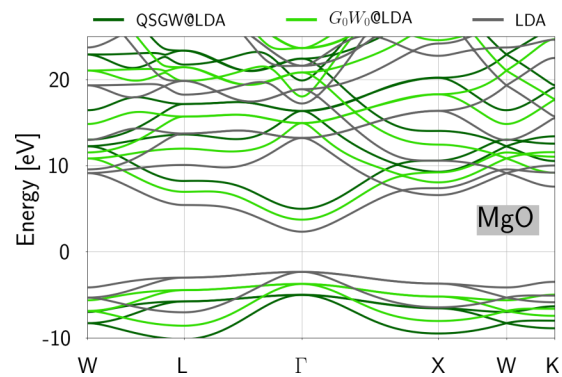

FIG. 1. Band structure of MgO calculated with QSGW (dark green), G_0W_0 (light green), and LDA (gray).

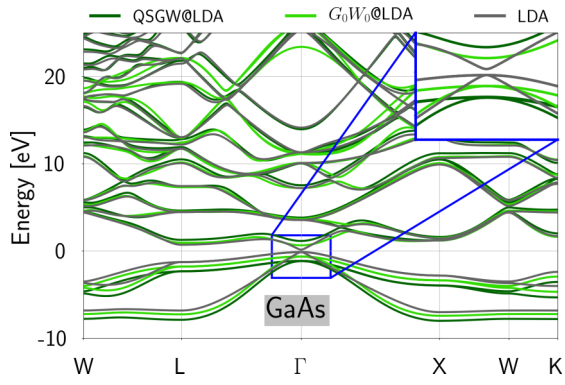

FIG. 2. Same as Fig. 1 for GaAs. The inset, framed in blue, shows the region around the fundamental (direct) band gap E_g.

example, the position of the 3*d* orbitals in GaAs shows substantial improvement upon self-consistency with respect to experiment. Taking the VBM (Γ_{1v} symmetry) as reference, the Ga 3*d* orbitals from QSGW are found 19.39–19.47 eV below it, in good agreement with an experimental value of 18.8 eV [42]. In contrast, the LDA position 14.94 eV below its VBM is ≈4 eV off. G_0W_0 lowers the LDA energy value to 16.43 eV. The latter is a substantial but still insufficient improvement over LDA, and QSGW is obviously superior.

In some QSGW calculations, the changes in effective electron and hole masses with respect to LDA are very significant. For instance, in GaAs, shown in Fig. 2, QSGW not only shifts the band energies, but also changes slope and curvature, as observed in similar calculations for GaN [43] and GaAs [44]. In GaAs, the QSGW bands in the gap region (upper-right corner in Fig. 2) exhibit smaller curvature than those in Ref. [45]. However, in that work, the QSGW implementation is different in that the optimized potential $v_{\rm xc}^{\rm opt}$ is mixed with the LDA potential, arguably leading to a mismatch with our results. The same discrepancy is obvious for the CBM reported in Ref. [44] where the authors indeed found that replacing a percentage of $v_{\rm xc}^{\rm opt}$ with the LDA potential reduces the effective mass. The amount was chosen such to reproduce the experimental band gap at 0 K. Without the mixing of potentials, a direct band gap, including spin-orbit coupling, ≈0.4 eV smaller than our result was obtained. Considering the SO correction to be ≈ 0.11 eV [14], there is a significant discrepancy remaining.

Finally, we get back to the possible reasons behind the overestimation of band gaps, indicating the intricate many-body effects in the different materials. Here we focus on three issues: (i) contributions from zero-point renormalization (ZPR), (ii) spin-orbit coupling (SOC) effects, and (iii) lack of vertex corrections.

(i) The impact of electron-phonon coupling varies even among tetrahedral *sp* semiconductors [41]. For instance, it plays an important role in diamond (ZPR correction of 0.41 eV for the fundamental band gap) while in Si, this correction only amounts to 0.06 eV, and for other materials it may be even neglected [35]. In all our calculations, atomic vibrations are not included, thus, the experimental data shown in Table I have been corrected such to exclude corresponding contributions as well. Importantly, the values reported in literature differ significantly and depend considerably on the method used, thus, their choice appears somewhat arbitrary. For Si and SiC, these corrections stem from LDA calculations [35]. For diamond, the calculated correction in Ref. [35] is 0.33 eV, while extrapolation of temperature-dependent experimental data returns 0.41 eV [46]. Note also that Antonius and coworkers [47] included many-body effects in the calculation of ZPR for diamond, leading to a correction of 0.628 eV. Considering the latter value, the remaining discrepancy of our results compared to experiment is 2% only.

In addition, in polar compounds, the longitudinal and transversal optical phonons cause a polarization, leading to a lattice contribution to the screening of the QP [48]. Including this contribution to the screened Coulomb interaction on top of QSGW results [49], a significant narrowing of the fundamental band gaps by 2.12 and 1.23 eV was found for LiF and MgO, respectively.

(ii) The inclusion of SOC in QSGW calculations appears in the literature in either a perturbative [44,50] or an iterative [26] correction to the optimized Hamiltonian. In the first scheme, the SOC term enters the converged QSGW Hamiltonian, to return corrected eigenvalues. Following this approach, all-electron linear muffin-tin orbital (LMTO) calculations [44] showed for GaAs a band splitting of 0.366 eV for the first conduction band at Γ, in contrast to Ref. [12] obtaining a value of 0.1 eV. Thus, like in the case of ZPR, the uncertainty from such corrections is significant. Since aside from GaAs, the SOC does not considerably alter results of our materials set, its omission is not considered a major source of error in our results.

(iii) Adopting the polarizability from the RPA corresponds to setting the vertex to one, i.e., neglecting higher-order interactions. Lack of electron-hole interaction leads to underestimated dielectric screening, which is reflected in the overestimation of band gaps [22]. To make up for this shortcoming, Chen and coworkers [23] included an exchange-correlation kernel in the polarizability, finding reduced QSGW band gaps in a vast number of semiconductors. These findings are backed by similar calculations with a different exchange-correlation kernel [24].

B. Electronic density

It is important to recall that the eigenvalue-only correction G_0W_0 was motivated by the argument that KS provides wave functions close enough to the QP wave functions [5]. However, for some cases, it was shown that they can differ considerably [32]. To investigate the impact of QP self-consistency on wave functions and chemical bonds, we study the electron density distribution ρ. More specifically, we analyze the charge-density difference $\Delta\rho$ between results from LDA and QSGW:

$$\Delta\rho(\mathbf{r}) = \rho^{\rm LDA}(\mathbf{r}) - \rho^{\rm QP}(\mathbf{r}). \tag{8}$$

$\Delta\rho$ is evaluated on a dense grid, consisting of 400 points in each spatial direction, which allows for a careful assessment of charge reallocation resulting from self-consistency. We

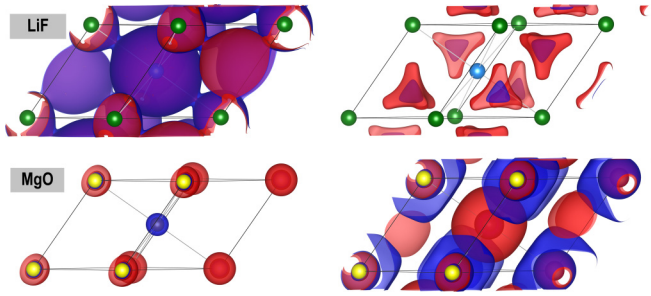

FIG. 3. Charge-density differences between QSGW and LDA results [Eq. (8)] for LiF (top) and MgO (bottom panels). On the left, the isovalue for both is $\pm 2 \times 10^{-2}$ e/bohrs^3; on the right, isovalues are $\pm 7 \times 10^{-3}$ e/bohrs^3 for LiF and $\pm 2 \times 10^{-3}$ e/bohrs^3 for MgO. Positive values are red, negative ones blue. Fluorine atoms are displayed in light blue, lithium in green, magnesium in yellow, oxygen in red (masked by isosurfaces).

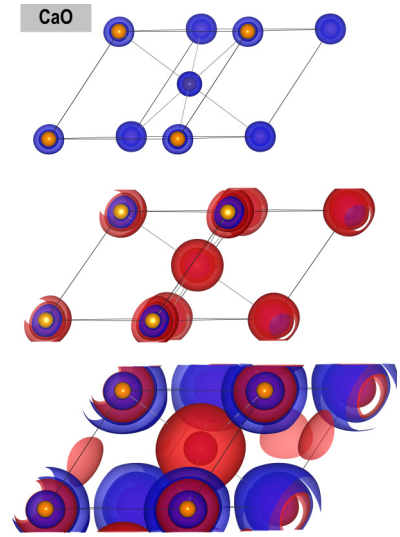

FIG. 4. Charge-density differences between QSGW and LDA results in CaO at isovalues of $\pm 2 \times 10^{-2}$ e/bohrs^3 (top), $\pm 1 \times 10^{-2}$ e/bohrs^3 (middle), and $\pm 2 \times 10^{-3}$ e/bohrs^3 (bottom), respectively. Orange spheres represent calcium, oxygen (red) sits at the center of the unit cell.

chose different isovalues, corresponding to a specific value of $\Delta\rho$ in space, in order to evaluate the degree of overlap between initial and final wave functions.

As first examples, we take two highly ionic compounds: LiF and MgO. In the top panels of Fig. 3, the charge-density differences for both materials at an isovalue of $\Delta\rho = \pm 0.02$ electron per cubic bohr are depicted. We infer that QSGW significantly redistributes density towards the nuclei. In the case of LiF (top), this effect comes at the expense of some density from the interatomic space. In contrast to MgO, at even higher isovalues, reallocation of electronic density is evident. In this regime (not shown), self-consistency makes F holding less charge in its surrounding, with density differences of the order of 1 electron per cubic bohr. In fact, Kaplan and coworkers [51] have shown that for LiF molecules, QSGW gives a dipole moment in good agreement with experiment, while DFT (using PBE) underestimates it. Exhibiting a clearly visible isosurface at ± 2 e/bohrs^3, the area surrounding the anion is most affected by self-consistency, demonstrating that Ψ^{LDA} overlaps poorly with Ψ^{QP}. This finding reflects our observation that the bottom of the valence band at the Γ point (here Li 1s) is lowered by 13 eV compared to its initial LDA value.

Density differences in the interstitial region are only present at very low scale. For both materials, we see in Fig. 3 a modest change in density upon self-consistency. At this small isovalue ($\pm$2–7 e/bohrs^3), the charge rearrangement is much less evident in LiF than in MgO. We conclude that the initial and final wave functions of MgO show considerable differences only at very low scales, in other words, overall they overlap to a large extent.

In general, $\Delta\rho$ is much higher valued, by two orders of magnitude, around the nuclei than in the space between them. This highlights the correction of the well-known delocalization error of (semi)local KS functionals [52,53] by QSGW. The only exception is the *immediate* neighborhood around the metal atom (Mg) which is less charged in QSGW than in LDA, as visible in the bottom panels of Fig. 3. Importantly, there is a large charge accumulation around the cations, while the region around oxygen is always slightly depleted. These last aspects are also present in our next example.

Although there are plenty of DFT calculations on calcium oxide (see Ref. [54] and references therein), this material has been less studied with MBPT methods [55]. Experimentally, x-ray spectra show that the charge density at a distance of 0.18 bohrs from the nucleus is roughly four times higher around calcium than around oxygen [56]. In LDA, the delocalization error hampers an accurate description of the proportion of electronic charge around the ions and is reflected in the O(2s) and O(2p) bandwidths, being by ≈ 0.5 eV larger than obtained by electron momentum spectroscopy measurements (EMS) [57]. Thus, one may wonder whether QSGW provides a solution to these shortcomings. Looking at the charge-density rearrangement at low isovalues (middle and bottom panels of Fig. 4), we observe that QSGW changes the degree of ionicity, i.e., the redistribution of charge density only occurs in the vicinity of the ions while the interstitial is not affected. At higher isovalues ($\pm 2 \times 10^{-2}$ e/bohrs^3, top panel), there is only very small charge depletion around both nuclei. Like in MgO, this indicates that the LDA wave functions are close to its QSGW counterpart. Overall, the above-mentioned discrepancy with experiment [56] is only partially solved, and more experimental work would help settling the issue. CaO and MgO (Fig. 3) differ in the sense that overall (see high isovalues), in contrast to Ca, Mg gains charge, but they are very similar at low isovalues. Reallocation of electronic density is more pronounced in LiF than in the two oxides, CaO and MgO, where only the immediate vicinity of the nuclei is affected. For all three materials, QSGW results show more charge density within the MT compared to LDA (differences between 0.5 and 0.7 e/bohrs^3), and a significant part of the gain is found at the anion.

For comparison, we show in Fig. 5 the difference in electronic density distribution between PBE0 and QSGW results for LiF and MgO. While MgO follows the same trend as above, i.e., QSGW giving a considerably different density

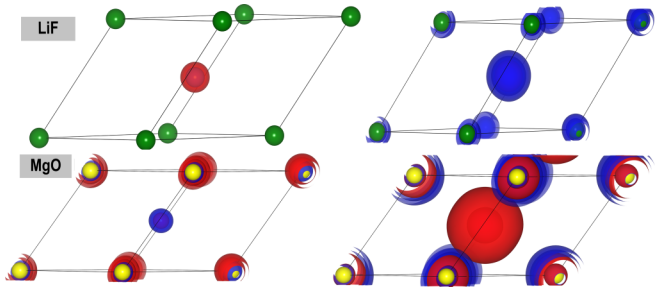

FIG. 5. Charge-density differences between QSGW and PBE0 results for LiF (top) and MgO (bottom panels). On the left, the isovalue is $\pm 2 \times 10^{-2}$ e/bohrs^3 for both materials; on the right, isovalues of $\pm 7 \times 10^{-3}$ e/bohrs^3 for LiF and $\pm 2 \times 10^{-3}$ e/bohrs^3 for MgO are chosen. Positive values are red, negative ones blue. F atoms are displayed in light blue, Li in green, Mg in yellow, O in red.

than PBE0, the situation is opposite in LiF. Here, the QSGW and PBE0 wave functions overlap to a large extent, and differences are only visible at small isovalues.

C. Starting-point (in)dependence

Clearly, the perturbative character makes the G_0W_0 method dependent on the underlying exchange-correlation functional. Self-consistency is supposed to cure this intrinsic flaw, as indeed found in the vast majority of works employing QSGW for different materials, as discussed in more detail below. An exception to this trend was reported by Liao and Carter [58] who found a considerable starting-point dependence of QSGW for hematite Fe_2O_3. To explore this issue, we investigate Ar, SiC, and C, materials that are characterized by very different band gaps. Three distinct initial choices of the exchange-correlation potential are employed, i.e., the LDA, the hybrid functional PBE0, and the Hartree-Fock approximation (HFA). As strikingly evident from Fig. 6 for the example of argon, the QP eigenvalues are practically the same in all three final band structures. The same holds for the indirect band gap along Γ-X and the direct gap at Γ in diamond and silicon carbide, where the different starting points lead to almost negligible differences (see Table II). One would expect that the closer the underlying result is to the final value, the faster should be the convergence behavior. Indeed, the calculation for the insulator argon profits from the HFA as the starting point, where only three iterations are required. Here, the initial (direct) band gap E^0_Δ is 14.96 eV, very close to the converged value of 15.33 eV. Yet, the same is not true for the band gap of diamond, where PBE0 as starting point takes more iterations to converge than the LDA case, despite the fact that the initial PBE0 value is 1 eV closer to the final value. Most counterintuitive is the case of SiC, where the fastest convergence is found for QSGW@LDA, starting from 1.25 eV, compared to QSGW@PBE0 starting from 2.77 eV. In fact, QSGW@HF starts from the huge value of 5.16 eV but still converges faster than QSGW@PBE0. Our findings are in contrast to all-electron calculations for small molecules by Koval and coworkers [61], where QSGW@LDA and QSGW@HF took the same number of iterations to converge.

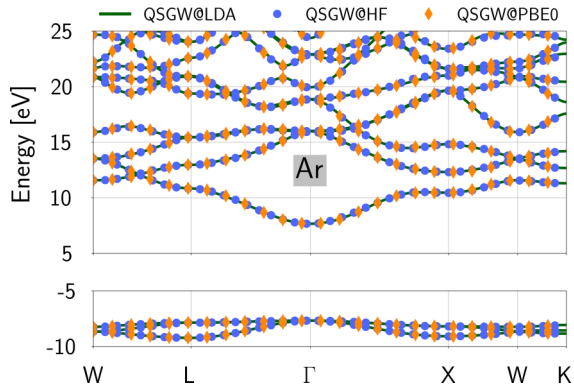

FIG. 6. Band structure of argon calculated with QSGW@LDA (green line), QSGW@PBE0 (orange diamonds), and QSGW@HF (blue circles).

From our findings summarized in Table II, we conclude that in the considered cases, self-consistency cures the dependence on the initial G_0, despite the considerable differences in initial eigenvalues, concerning both the DFT starting point as well as G_0W_0 results. In line with our results, the starting-point *independence* has also been shown for other types of functionals. As an example, results for oxides on top of GGA + U revealed only a weak dependence on the amount of the Hubbard parameter U [62]. Another QSGW study for complex oxides [63] based on the Heyd-Scuseria-Ernzhof (HSE) functional with different amounts of exact exchange shows that all starting points return the same fundamental band gap. Also for molecules, the converged results on top of PBE0-like hybrid functionals remained unchanged for different proportions of exact exchange as found by Kaplan and coworkers [51]. Our observations for HFA and PBE0 complement these studies, conforming that QSGW results do not depend on the initial parametrization of the exchange-correlation potential. However, choosing the *right* starting point may save some

TABLE II. E_Δ (in eV) at high-symmetry points for C, SiC, and Ar together with the number of iterations until convergence. For comparison, the two last columns show the results of G_0W_0 calculations with EXCITING on top of LDA and PBE0, taken from Refs. [59,60].

		QSGW@LDA			QSGW@PBE0			QSGW@HF			G_0W_0@LDA	G_0W_0@PBE0
		E_Δ	Iterations	E^0_Δ	E_Δ	Iterations	E^0_Δ	E_Δ	Iterations	E^0_Δ	E_Δ	E_Δ
C	$\Gamma - X$	7.01	6	4.40	7.00	7	5.40	6.99	10	8.94	5.95	6.26
C	$\Gamma - \Gamma$	8.41		5.53	8.44		6.71	8.41		10.66	7.43	8.10
SiC	$\Gamma - X$	3.00	5	1.25	3.03	8	2.77	3.03	6	5.16	2.43	3.13
SiC	$\Gamma - \Gamma$	8.35		6.40	8.38		8.05	8.40		11.87	7.51	8.47
Ar	$\Gamma - \Gamma$	15.34	5	8.18	15.34	4	9.97	15.33	3	14.96	13.28	14.35

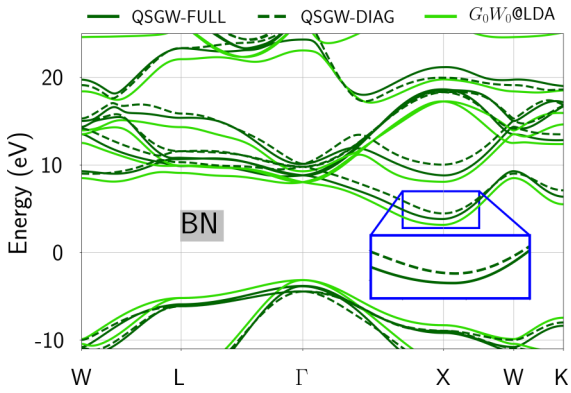

FIG. 7. QSGW band structure of BN using the full (solid line) and the diagonal self-energy matrix (dashed line). For comparison, the G_0W_0 results (light green) are included.

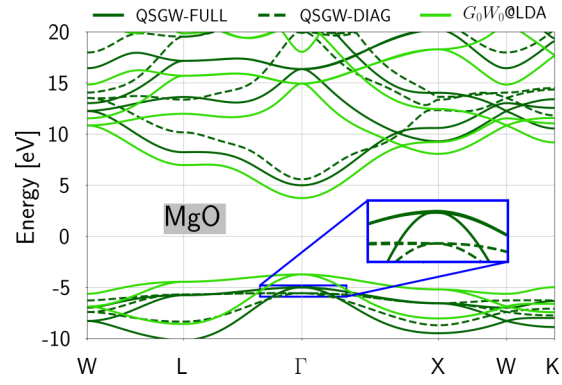

FIG. 8. Same as Fig. 7 for MgO.

iterations in this computationally very involved scheme, like seen in the case of argon.

D. Effect of off-diagonal matrix elements

In this section, we look into the impact of off-diagonal matrix elements, referred to as *nl* terms. Their role has been discussed in literature, albeit not extensively. In contrast to G_0W_0, this feature couples different bands in the self-energy, as evident from Eq. (1). To investigate its influence on the electronic structure, we perform QSGW calculations for Ar, SiC, C, MgO, and BN with (i) diagonal elements only ($n = l$) and (ii) the full self-energy matrix (standard QSGW, $n \neq l$).

Based on these results, we conclude that the degree at which *nl* terms affect the band structure is strongly material dependent. For example, for simple *sp* semiconductors, such as SiC, the effect is less dramatic than in more correlated systems [64]. More specific, the fundamental band gap of SiC is 3.87 eV in the diagonal case, compared to 3.00 eV when including off-diagonal contributions. In diamond, the effect is even less pronounced but dependent on the segment of the Brillouin zone. In contrast, in all other materials investigated here, the band gap is slightly widened. The indirect band gap including *nl* terms is 7.01 eV, only 0.14 eV larger than in the diagonal case (6.87 eV). Contrary to our overall findings, Shishkin and coworkers [31] reported *increased* band gaps upon inclusion of *nl* terms. The impact of off-diagonal terms depending on the degree of correlation had also been observed for a perturbative correction to LDA eigenvalues [33].

Analyzing our results for BN and MgO, shown in Figs. 7 and 8, it is clear that removal of the *nl* terms opens the gaps. Like in SiC (not shown), in BN the overall shape of the bands is not significantly changed by the off-diagonal terms, but they matter when it comes to details. Omitting them shifts the conduction band upwards and the valence band downwards, thus widening both the indirect and the direct band gaps by 1.3 and 1.6 eV, respectively. In this material, we also notice that a number of band crossings in the conduction band are present or absent in one case with respect to the other.

According to our results, the *nl* terms also play an important role in the band curvature, i.e., effective masses. The first conduction band in BN exemplifies this effect, also showing a dependence on the direction in **k** space, observed in other calculations as well [65]. Looking at the CBM (inset in Fig. 7), in the full-matrix case the slope along the X-W direction is steeper than in the diagonal-matrix counterpart, while it exhibits less variation in other directions. This indicates an enhanced anisotropy of the charge-carrier mobility. Likewise, the slope at the VBM flattens noticeably when excluding *nl* terms, i.e., making the effective hole mass heavier and thus charge carriers less mobile. This feature is also present at the VBM of MgO (see inset of Fig. 8).

While we observe a striking effect of *nl* terms in our results, the extent of their impact has been debated in literature [31,51]. Analytical considerations [19] indicate that the contributions from *nl* terms are very small compared to the diagonal elements showing scaling behaviors of η^{-3} and η^{-1}, respectively [see Eq. (7), Sec. IV B]. In our results, these terms are indeed much smaller than the diagonal elements. But, however small the off-diagonal values are compared to the diagonal elements, we still observe a clear impact on the whole band structure.

To exemplify the ratio between diagonal and off-diagonal matrix elements, we first focus on the VBM in BN and diamond, consisting of three *degenerate* states in both cases. For highlighting their respective impact, we only compute the contributions from mixing these states, i.e., using the matrix elements $\langle n|\Sigma_{\mathrm{xc}}(\epsilon_n) - v_{\mathrm{xc}}|l\rangle$, with $\epsilon_l = \epsilon_n$. While the diagonal components $\Sigma_{nn}(\epsilon_n)$ for both materials are of the order 10^{-1} Ha, these degenerate *nl* terms are two orders of magnitude smaller, inline with Ref. [19]. Second, we consider the matrix elements between the degenerate VBM and the nondegenerate CBM. Here, BN and diamond show considerable differences. While in BN, the corresponding *nl* terms have magnitudes up to 10^{-2} Ha, the maximum value in diamond is of the order of 10^{-4} Ha only. This indicates that this issue is more complex, depending on material and specific states.

In some cases, unphysical features may arise when neglecting the *nl*-terms. Among these materials, argon shows the most pronounced effect by adopting an indirect band gap, when starting from LDA, exhibiting a direct band gap and the VBM located at the Γ point, as shown in Fig. 9. Including *nl* terms moves the VBM back to this high-symmetry point, and thus gives a direct QSGW band gap, like observed in ex-

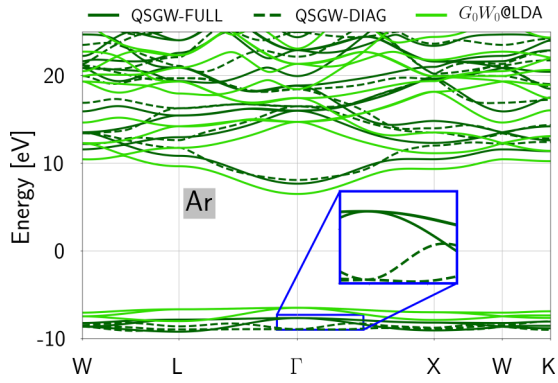

FIG. 9. Same as Fig. 7 for Ar.

periments. In fact, Bruneval and coworkers [32] compared the LDA and QSGW wave functions of argon, showing that away from high-symmetry points, the overlap between them is poor for the conduction bands. Interestingly, even for this weakly bound material, with atomiclike orbitals, off-diagonal matrix elements, i.e., mixing of states, are apparently necessary for the proper description of the band structure. We note that the same effect is observed in GaAs (not shown here). Using a *GW* scheme similar to QSGW but to first iteration only, Aguilera and coworkers [66] concluded that in some topological insulators, leaving out the *nl* terms in the self-energy leads to "unphysical band dispersion in those parts of the Brillouin zone where the bands hybridize strongly." In addition, the *nl* terms in QSGW have proven to be also crucial to properly describe electronic states in molecules [51].

IV. IMPLEMENTATION

A. The (L)APW + LO basis

For solving the KS equations, the unit cell is divided into two types of volumes. The *muffin-tin* (MT) region consists of nonoverlapping spheres with radii R^{α}_{MT}, centered at the nuclear positions $\mathbf{r}_{\alpha}$, where the index α indicates the atom. The remaining part is called *interstitial region* [67]. This division of space goes hand in hand with a dual basis, where in the interstitial region plane waves (PWs) are used to represent KS functions, density, and potential. In the MT spheres atomiclike functions account for the rapidly varying potential near the nuclei. Obviously, such functions can equally well represent valence and core states.

More specifically, in a unit cell of volume Ω, the basis functions are defined as

$$\phi_{\mathbf{k}+\mathbf{G}}(\mathbf{r}) = \begin{cases} \frac{1}{\sqrt{\Omega}} e^{i(\mathbf{k}+\mathbf{G})\cdot\mathbf{r}}, & \mathbf{r} \in I \\ \phi^{\mathrm{LAPW}}_{\mathbf{k}+\mathbf{G}}(\mathbf{r}) = \sum_{l,m} \left[A^{\zeta}\, u^{\alpha}_{l}(r^{\alpha}; E_{l\alpha}) + B^{\zeta}\, \dot{u}^{\alpha}_{l}(r^{\alpha}; E_{l\alpha})\right] Y^{m}_{l}(\widehat{\mathbf{r}^{\alpha}}), & \mathbf{r} \in \mathrm{MT} \end{cases} \tag{9}$$

with the vector $\mathbf{r}^{\alpha} = \mathbf{r} - \mathbf{r}_{\alpha}$. Y^{m}_{l} are spherical harmonics, and l and m the azimuthal and the magnetic quantum number, respectively. The label ζ gathers the parameters $\mathbf{k}+\mathbf{G}$, l, m, and α. The $u^{\alpha}_{l}(r^{\alpha}; E_{l\alpha})$ are solutions of the radial Schrödinger equation for the spherically symmetric part of the potential in the respective atomic sphere.

The *linearization energies* $E_{l\alpha}$ are chosen such to lie within the band of the respective character, where deviations from the actual KS energy are accounted for by the term $\dot{u}$, i.e., the derivative of the radial function with respect to energy [68,69]. The fixed $E_{l\alpha}$ makes the basis functions energy independent, and the secular equation represents a linear eigenvalue problem (hence the term "linearized" in the name). The coefficients A and B ensure continuity of the basis functions at the sphere boundary. Since the inclusion of $\dot{u}$ impacts the form of the basis functions within the MT, the LAPW method demands a rather large number of basis functions to restore the proper shape of the eigenstates close to the nuclei [70,71].

Alternatively, one can linearize the eigenvalue problem by using the radial function only, and add a *local orbital* (LO) at the respective linearization energy. This so-called APW + LO method [72] allows for more flexibility of the basis at lower cost. Note that in the following, for brevity, we use the term LAPW for both ways of linearization. Local orbitals ϕ^{LO}_{μ} are defined within the MT as

$$\phi^{\mathrm{LO}}_{\mu}(\mathbf{r}) = \delta_{\alpha\alpha_{\mu}}\delta_{ll_{\mu}}\delta_{mm_{\mu}}\left[a_{\mu}\, u^{\alpha}_{l}\left(r^{\alpha}; E^{\mathrm{LO}}_{l\alpha}\right) + b_{\mu}\, \dot{u}^{\alpha}_{l}\left(r^{\alpha}; E^{\mathrm{LO}}_{l\alpha}\right)\right] Y^{m}_{l}(\widehat{\mathbf{r}^{\alpha}}). \tag{10}$$

Local orbitals are also used for extended core (i.e., semicore) states as well as high-energy states, the latter being crucial for obtaining accurate *GW* results [73]. Also second- or higher-order derivatives may enter the linear combination in Eq. (10). The coefficients a_{μ} and b_{μ} ensure normalization and that ϕ^{LO}_{μ} goes to zero at the boundary.

The product of two KS functions $\psi_{n\mathbf{k}}$ often appears in the matrix form of nonlocal operators. To represent these products, we make use of the *mixed product basis* $\{\chi^{\mathbf{q}}_{i}\}$, or MB for short [14,15,17],

$$\psi_{n\mathbf{k}}(\mathbf{r})\psi^{*}_{m\mathbf{k}-\mathbf{q}}(\mathbf{r}) = \sum_{i} M^{i}_{nm}(\mathbf{k},\mathbf{q})\chi^{\mathbf{q}}_{i}(\mathbf{r}) \tag{11}$$

with coefficients

$$M^{i}_{nm}(\mathbf{k},\mathbf{q}) \equiv \int_{\Omega} \left[\chi^{\mathbf{q}}_{i}(\mathbf{r})\psi_{m\mathbf{k}-\mathbf{q}}(\mathbf{r})\right]^{*} \psi_{n\mathbf{k}}(\mathbf{r})\, d\mathbf{r}, \tag{12}$$

where n and m are band indices and i labels the MB function. Frequency-(in)dependent two-body operators are represented in matrix form as $O_{ij}(\mathbf{r},\mathbf{r}';\omega)$:

$$O_{ij}(\mathbf{q},\omega) = \int_{V} \left[\chi^{\mathbf{q}}_{i}(\mathbf{r})\right]^{*} O(\mathbf{r},\mathbf{r}';\omega)\chi^{\mathbf{q}}_{j}(\mathbf{r}')\, d\mathbf{r}\, d\mathbf{r}' \tag{13}$$

where $V = N_c\Omega$ is the crystal volume with N_c being the number of unit cells. The Bloch functions $\chi^{\mathbf{q}}_{i}$ are normalized to unity within V.

Following the spirit of the LAPW method, the construction of the MB functions employs space partitioning between the

MT spheres and the interstitial region such that $\chi_i^{\mathbf{q}}$ belongs to either the former or the latter space. This gives rise to two types of MB functions, i.e., products of plane waves [74] and products of radial functions (from the same MT sphere), $\nu_{\alpha NL}(r^\alpha)$, times spherical harmonics. The radial product functions are neither normalized nor orthogonal. To ensure linear independence of these products, we diagonalize their overlap matrix [15], returning a set of eigenvalues and eigenvectors $\{\lambda_N, c_{ll',N}\}$. If the eigenvalue is lower than a given threshold, the corresponding eigenvector is assumed to be linearly dependent and discarded [15,75]. The final product $\nu_{\alpha NL}(r^\alpha)$ consists of a linear combination of the eigenvectors corresponding to selected eigenvalues and radial functions. For being selected, the radial functions u_l and $u_{l'}$ have to fulfill two conditions [17]: (i) l and l' must be smaller than a predefined threshold $l_{\max}^{\mathrm{MB}}$, and (ii) the triangular condition $|l-l'| \leqslant L \leqslant l+l'$ must be met. The product of two spherical harmonics can be expanded into spherical harmonics Y_L^M. For each wave vector $\mathbf{q}$, considering translation symmetry, we arrive at the product basis for the MT:

$$\gamma_{\alpha NLM}^{\mathbf{q}}(\mathbf{r}) = e^{i\mathbf{q}\cdot\mathbf{r}_\alpha}\nu_{\alpha NL}(r^\alpha)Y_L^M(\hat{\mathbf{r}}^\alpha). \tag{14}$$

The set $\{\nu_{\alpha NL}\}$ does not include the derivatives of u_l's due to their negligible contribution [15], i.e., $B_{lm}^{\mathbf{G}+k}$ in Eq. (9) is set to zero. However, we include the energy derivatives $\dot{u}_l^\alpha(r^\alpha; E_{l\alpha})$ stemming from local orbitals by incorporating them in the coefficients of the expansion at the left in Eq. (12). Radial functions along with their integrals, and hence $\{\nu_{\alpha NL}\}$, are initialized only once and remain fixed afterwards.[2]

Analogous to the product of radial functions, we calculate the overlap matrix of the plane-wave products, with eigenvalues λ_i and eigenvectors $S_{\mathbf{G}i}$. For each wave vector $\mathbf{q}$, the interstitial basis function in the MB is

$$P_i^{\mathbf{q}}(\mathbf{r}) \equiv \frac{1}{\sqrt{\Omega}}\sum_{\mathbf{G}}^{G_{\max}} \tilde{S}_{\mathbf{G}i}e^{i(\mathbf{q}+\mathbf{G})\cdot\mathbf{r}}\,\theta(\mathbf{r}), \tag{15}$$

with $\tilde{S}_{\mathbf{G}i} \equiv S_{\mathbf{G}i}/\sqrt{\lambda_i}$, and the step function $\theta(\mathbf{r})$ guarantees that the integral is zero if $\mathbf{r}$ resides outside the interstitial region. Finally, the MB is given as follows:

$$\left\{\chi_i^{\mathbf{q}}(\mathbf{r})\right\} = \left\{\gamma_{\alpha NLM}^{\mathbf{q}}(\mathbf{r}), P_i^{\mathbf{q}}(\mathbf{r})\right\}. \tag{16}$$

Crucial for the calculation of the self-energy and the polarizability matrix are the expansion coefficients M_{nm}^i, obtained by inserting Eq. (16) into (12).

B. QSGW in EXCITING

The QSGW implementation involves several operators in matrix form, classified in three groups:

(i) *Group A:* Operators making up the Hamiltonian H_0. For details, we refer to Ref. [76].

(ii) *Group B:* Nonlocal operators, appearing in Hedin's equations. The implementation in EXCITING follows closely Ref. [17], albeit with some differences.

[2]Including the updated density from the optimized H_0 into the local potential V_α in the radial part of the Schrödinger equation worsened the results in some cases.

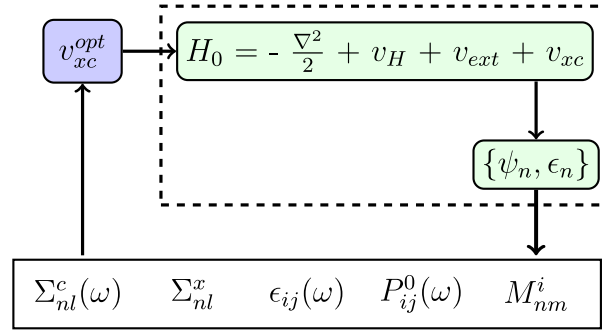

FIG. 10. Flowchart of the QSGW implementation in EXCITING. Green (white) color refers to operators from group A (B); blue indicates the only representative of group C.

(iii) *Group C:* The nonlocal exchange-correlation potential $v_{\mathrm{opt}}^{\mathrm{xc}}$ [see Eq. (1)].

Figure 10 sketches the implementation of the QSGW method in EXCITING. The green blocks represent operators from group A and the output of the secular equation, i.e., the eigenvectors and eigenvalues; the blue block contains the optimized potential (group C). The bottom block displays the main quantities from group B. Step one of the implementation is to perform an IP calculation with a chosen exchange-correlation potential v^{xc} and operators from group A, providing the initial eigenvectors and energies. Then, the operators from group B are built in the MB, i.e., the screened Coulomb interaction $W_{ij}(\omega)$, the polarizability $P_{ij}^0(\omega)$, the bare Coulomb interaction v_{ij}, and the dielectric matrix $\epsilon_{ij}(\omega)$. The optimized potential in matrix form is then computed according to Eq. (1). Its diagonal and off-diagonal matrix elements are expressed in terms of KS functions, and thus expressed in terms of the LAPW basis in order to be inserted in the Hamiltonian. Step two is to replace the initial v^{xc} from the IP scheme with $v_{\mathrm{opt}}^{\mathrm{xc}}$. Keeping this potential fixed, the secular equation is solved for each $\mathbf{k}$ point using the updated H_0. This includes an iterative procedure, called *inner cycle*, indicated by dashed lines in the figure. With the eigenvectors and eigenvalues produced in the inner cycle, in the third step, the matrix operators from groups B and C are recalculated. The new potential $v_{\mathrm{opt}}^{\mathrm{xc}}$ is plugged into H_0, and steps 2 and 3 are repeated until convergence. This eventually leads to the transition from the initial KS eigenfunctions to the QP states via $\{\psi_{n\mathbf{k}}^{\mathrm{IP}}, \epsilon_{n\mathbf{k}}^{\mathrm{IP}}\} \rightarrow \{\psi_{n\mathbf{k}}, \epsilon_{n\mathbf{k}}\} \rightarrow \{\psi_{n\mathbf{k}}^{\mathrm{QP}}, \epsilon_{n\mathbf{k}}^{\mathrm{QP}}\}$. The complete procedure is called the *outer cycle*.

For consistency, (i) the $\mathbf{q}$ grid and the $\mathbf{k}$ grid are common to both cycles (unlike other implementations [14]), (ii) in all operators we consider the same number of unoccupied states, (iii) *all* core electrons enter the self-energy operator, and (iv) all operators are based on the same computational parameters, i.e., $E_{l\alpha}$, $R_\alpha^{\mathrm{MT}} \cdot |\mathbf{k}+\mathbf{G}|_{\max}$. An exception is the self-consistency criterion for the charge density which typically is much stricter in the inner than the outer cycle.

The Coulomb-interaction matrix in the MB has three distinctive blocks, namely, the two where both χ_i and χ_j are either $\in$ MT or $\in I$, and a third one where $\chi_i \in$ MT and $\chi_j \in I$. More details are given in Refs. [17,75]. The diagonal form of the Coulomb matrix is not only convenient for simplifying

the matrix multiplication. Also, when computing the dielectric matrix, the singularity at $\mathbf{q} = 0$ is getting restricted to the first matrix element (head, H) and the first column and row (wings, W), while the rest (body, B) holds no singularity. Seeking to recover this diagonal matrix form of response functions, the MB has to undergo a basis transformation [75], using the fact that a Hermitian operator is diagonal in the basis of its eigenvectors. Hence, in the unitary transformation

$$|\chi^{\mathbf{q}}_{\mu}\rangle = \sum_{i} |\chi^{\mathbf{q}}_{i}\rangle U^{\mathbf{q}}_{\mu i}, \tag{17}$$

the matrix U is expressed in a *v-diagonal basis* [75], where $U^{\mathbf{q}}_{\mu i}$ is the ith component of the μth eigenvector of the Coulomb interaction matrix $v_{ij}(\mathbf{q})$. We stress that this transformation does not imply an approximation. In practice, we consider only physically significant eigenvectors, i.e., those whose eigenvalues are above a threshold [75]. In our QSGW implementation, the chosen threshold remains fixed, yet the number of eigenvectors taken into account varies but typically stabilizes after a few iterations.

The dielectric function includes an integral over the product of the polarizability and the bare Coulomb interaction. The latter introduces a numerical challenge due to above-mentioned singularity as $\mathbf{q}$ goes to zero, but is alleviated by means of the v-diagonal basis. We then treat the $q = 0$ term of the dielectric matrix within $\mathbf{k} \cdot \mathbf{p}$ theory [77] for evaluating H, W, and B, as detailed in Ref. [17]. Throughout the implementation, we use a contraction between the square root of the Coulomb matrix and the coefficients $M^{i}_{nm}(\mathbf{k}, \mathbf{q})$ in the v-diagonal basis representation (note the greek indices introduced with the basis transform):

$$\tilde{M}^{\mu}_{nm}(\mathbf{k}, \mathbf{q}) \equiv \sqrt{v_{\mu}(\mathbf{q})} M^{\mu}_{nm}(\mathbf{k}, \mathbf{q}), \tag{18}$$

where $v_{\mu}(\mathbf{q})$ are the eigenvalues of the Coulomb matrix.

In contrast to G_0W_0, in QSGW the self-energy is not diagonal. Exchange and correlation self-energies include a mixing of states, embodied in the off-diagonal terms of the respective matrices. Expectation values taken with respect to two different states, i.e., n and l, make up the upper triangle of the self-energy matrix, the lower one is constructed by enforcing Hermiticity. In the following, these off-diagonal elements are denominated *nl terms*. The exchange part is calculated as suggested by Betzinger and coworkers [16].

Evaluation of the correlation self-energy $\Sigma^{c}(\omega)$ is the most involved part in our implementation. We use the correlation term of the screened Coulomb potential $W^{c}(\omega) = W(\omega) - v$, replace $G_0(\omega + \omega')$ with its Lehman representation in the KS basis, insert the MB expansion of $W^{c}(\omega)$, and finally employ the definition of $M^{i}_{nm}(\mathbf{k}, \mathbf{q})$ from Eq. (12). Following these steps, the matrix elements of the correlation self-energy $\Sigma^{c}_{nl\mathbf{k}}(\omega) = \langle \psi_{n\mathbf{k}} | \Sigma^{c}(\omega) | \psi_{l\mathbf{k}} \rangle$ become

$$\Sigma^{c}_{nl\mathbf{k}}(\omega) = \frac{1}{N_c} \frac{i}{2\pi} \sum_{\mathbf{q}}^{\mathrm{BZ}} \sum_{m} \sum_{i,j} \times \int_{-\infty}^{\infty} \frac{\left[M^{i}_{nm}(\mathbf{k}, \mathbf{q})\right]^{*} W^{c}_{i,j}(\mathbf{q}, \omega') M^{j}_{lm}(\mathbf{k}, \mathbf{q})}{\omega + \omega' - \tilde{\epsilon}_{m\mathbf{k}-q}} d\omega'. \tag{19}$$

In the above equation, $\tilde{\epsilon}_{n\mathbf{k}} \equiv \epsilon_{n\mathbf{k}} + i\eta\, \mathrm{sgn}(\epsilon_F - \epsilon_{n\mathbf{k}})$. Writing $W^{c}_{i,j}(\mathbf{q}, \omega)$ in the v-diagonal basis and using the contraction in Eq. (18), we obtain the product

$$M^{*} W^{c} M = \sum_{\mu\nu} \left[\tilde{M}^{\mu}_{nm}(\mathbf{k}, \mathbf{q})\right]^{*} \left[\epsilon^{-1}_{\mu\nu}(\mathbf{q}, \omega') - \delta_{\mu\nu}\right] \tilde{M}^{\nu}_{lm}(\mathbf{k}, \mathbf{q}). \tag{20}$$

For the off-diagonal matrix elements, this is a three-dimensional matrix whose size depends on the number of frequencies, number of states (unoccupied, valence, and core states), and total number of *nl* terms. Because the convolution integral over frequency in Eq. (19) has poles infinitesimally close to the real axes, a large number of frequencies are required to achieve precise results.

The evaluation of Eq. (20) is performed using the imaginary-frequency formalism, i.e., by replacing $\omega = iu, \omega' = iu'$, where u and u' are real. Correspondingly, both the screened Coulomb potential W and the G_0W_0 self-energy Σ are computed along the imaginary frequency axis. The self-energy along the real axis is then obtained by means of the Padé approximants [78]. For technical details regarding the numerical implementation of the frequency convolution integral [Eq. (20)], we refer to Ref. [17]. From a practical point of view, the formalism leads to quickly converging results with respect to the frequency grid. Unfortunately, the analytical-continuation technique for mapping back from the imaginary to the real axis is known to suffer from deficiencies, e.g., when treating core states or computing molecules [11]. Nevertheless, employing the Padé approximants has been verified to produce stable and reliable results for the chosen bulk systems. For future work, the contour deformation technique [79] may be implemented to evaluate the convolution integral.

In the EXCITING code, the hybrid *message passing interface* (MPI) + shared-memory multithreading (OpenMP) parallelization is used. Computation of $(\mathbf{k}/\mathbf{q})$-dependent quantities is efficiently parallelized with MPI, whereas the computations of the self-energy matrix elements make use of the OpenMP technology.

V. CONCLUSIONS

In summary, we have adopted and adapted the QSGW formalism to the full-potential (L)APW + LO framework and implemented it into the all-electron package EXCITING. This allowed us to study the electronic structure of selected materials. We have observed an overall overestimation of band gaps, however, there is good agreement with experiment, when corrections for zero-point vibrations and spin-orbit coupling are considered. We have found significant impact of QP self-consistency on band dispersions and effective masses. For the examples of LiF, MgO, and CaO, we have shown considerable reorganization of electronic charge surrounding the ions compared to LDA densities, where the actual extent of the effect depends on the material. Addressing the issue of starting-point (in)dependence for different initial potentials, we have found the final results to be in excellent agreement. Finally, we have analyzed the impact of off-diagonal terms in the self-energy matrix on the electronic structure. These contributions to the optimized potential prove important in most cases. For example, in argon, they are crucial for obtain-

TABLE III. Total number of LOs for the materials considered in this work.

	SiC	Si	BN	GaAs	MgO	CaO	LiF	Ar	C
Number of LOs	155	164	138	312	168	136	140	127	146

ing the right character of the band gap. Our implementation in an all-electron framework and our results for prototypical materials are paving the way for calculations of more complex compounds.

ACKNOWLEDGMENTS

This work was mainly supported by the International Max Planck Research School (IMPRS) for Functional Interfaces in Physics and Chemistry. Partial funding by the Caroline von Humboldt–Stipendienprogramm of the HU Berlin and by the Deutsche Forschungsgemeinschaft (DFG, Project No. 182087777-SFB 951) is appreciated. We thank M. von Schilfgaarde for very helpful discussions and hosting N.S.-I. during a research visit to his group at King's College, London. The Wannier interpolation of the band structures was implemented by S. Tillack. N.S.-I. gratefully acknowlegdes technical support by A. Gulans and R. Pela.

APPENDIX A: CONFIGURATION OF LOCAL ORBITALS

In all calculations, we enhance the (L)APW basis set by a large number of LOs (indicated in Table III) to represent low-energy (semicore) as well as unoccupied states. They cover a broad range of energy parameters (see examples in Table IV). Previous G_0W_0 calculations with EXCITING [73] showed that convergence within 3-meV precision with respect to the number of LOs is reached when six l channels are included. Based on these results, we set $l^{\mathrm{LO}}_{\mathrm{max}} = 6$ for all materials. A particular case is GaAs where about twice the number of LOs is required compared to the average of the other materials.

Since the radial functions are fixed in our QSGW implementation, the choice of linearization energies $E_{l\alpha}$ requires special care. As an example, Table IV presents the setup of LOs for the first three l channels for GaAs. We adjust the notation from Sec. IV A [Eq. (10)], leaving out the subscript α and adding instead the index i to the linearization energy E_{il}. We search for these energies *prior* to the calculation by an automatized optimization procedure based on the Wigner-Seitz rules [80]. Some of them (marked in Table IV by the superscript t) are further optimized after the first QSGW iteration (and frozen afterwards). For GaAs, LOs with l^{LO} between 3 and 6 are linear combinations without derivatives of u_l, and the number of LOs for the channels $l^{\mathrm{LO}} = 5, 6$ is two. In general, we include LOs with energies up to 22 Ha.

APPENDIX B: COMPUTATIONAL PARAMETERS

The crystal structures and lattice parameters, as well as the muffin-tin radii R^{MT}_{α}, for all systems calculated in this work are specified in Table V. G_0W_0 and QSGW calculations are performed on a $4 \times 4 \times 4$ **k**-point grid, whereas IP calculations employed a $6 \times 6 \times 6$ **k** grid. In the binary compounds, the R^{MT}_{α} are, with the exception of calcium oxide, chosen to be the same for both elements. For the calcium atom, the description of the nodal structure of $4p$ orbitals requires either a large amount of PWs or a large R^{MT}, for which we choose the latter option, while for oxygen a smaller radius is sufficient. The product $R^{\mathrm{MT}} \cdot |\mathbf{G} + \mathbf{k}|_{\mathrm{max}}$, which determines the number of PWs in the basis set, is set to either 10 or 11, values that guarantee high numerical precision. For the radial functions, we set the maximum azimuthal number $l^{\mathrm{APW}}_{\mathrm{max}}$ to 12 for all materials. For products of radial functions (see Sec. IV A), we discard eigenvectors of the overlap matrix whose eigenvalues are below 1×10^{-4}. In this implementation, we restrict the radial functions entering the MB by a cutoff parameter $l^{\mathrm{MB}}_{\mathrm{max}} = 3$, without loss of precision.

TABLE IV. Configuration of the three LOs with lowest energy for $l^{\mathrm{LO}} = 0$, 1, and 2 in GaAs. The second column shows the radial part of the LO, the right column the linearization energy E_{jl} (in Ha) for index j and angular momentum l. The index μ, and the coefficients a_μ and b_μ, which are distinct for every LO, were introduced in Sec. IV A.

l	Ga	
	$a_\mu\, u_0(\mathbf{r}', E_{10}) + b_\mu\, \dot{u}_0(\mathbf{r}', E_{10})$	$E_{10} = -5.08095^t$
s	$a_\mu\, \dot{u}_0(\mathbf{r}', E_{20}) + b_\mu\, \ddot{u}_0(\mathbf{r}', E_{20})$	$E_{20} = -0.3695^t$
	$a_\mu\, u_0(\mathbf{r}', E_{10}) + b_\mu\, u_0(\mathbf{r}', E_{20})$	
	$a_\mu\, u_1(\mathbf{r}', E_{11}) + b_\mu\, \dot{u}_1(\mathbf{r}', E_{11})$	$E_{11} = 0.32460^t$
p	$a_\mu\, \dot{u}_1(\mathbf{r}', E_{11}) + b_\mu\, \ddot{u}_1(\mathbf{r}', E_{11})$	
	$a_\mu\, u_1(\mathbf{r}', E_{11}) + b_\mu\, u_1(\mathbf{r}', E_{21})$	$E_{21} = -0.36955^t$
	$a_\mu\, u_2(\mathbf{r}', E_{12}) + b_\mu\, \dot{u}_2(\mathbf{r}', E_{12})$	$E_{12} = -0.3695^t$
d	$a_\mu\, \dot{u}_2(\mathbf{r}', E_{12}) + b_\mu\, \ddot{u}_2(\mathbf{r}', E_{12})$	$E_{22} = 0.0000$
	$a_\mu\, u_2(\mathbf{r}', E_{22}) + b_\mu\, \dot{u}_2(\mathbf{r}', E_{31})$	$E_{32} = 1.3454$
l	As	
	$a_\mu\, u_0(\mathbf{r}', E_{10}) + b_\mu\, \dot{u}_0(\mathbf{r}', E_{10})$	$E_{10} = -0.3000^t$
s	$a_\mu\, \dot{u}_0(\mathbf{r}', E_{10}) + b_\mu\, \ddot{u}_0(\mathbf{r}', E_{10})$	
	$a_\mu\, u_0(\mathbf{r}', E_{10}) + b_\mu\, u_0(\mathbf{r}', E_{20})$	$E_{20} = -6.5840^t$
	$a_\mu\, u_1(\mathbf{r}', E_{11}) + b_\mu\, \dot{u}_1(\mathbf{r}', E_{11})$	$E_{11} = 0.0837^t$
p	$a_\mu\, \dot{u}_1(\mathbf{r}', E_{11}) + b_\mu\, \ddot{u}_1(\mathbf{r}', E_{11})$	
	$a_\mu\, u_1(\mathbf{r}', E_{11}) + b_\mu\, u_1(\mathbf{r}', E_{21})$	$E_{21} = -4.5224^t$
	$a_\mu\, u_2(\mathbf{r}', E_{12}) + b_\mu\, \dot{u}_2(\mathbf{r}', E_{12})$	$E_{12} = -1.1219^t$
d	$a_\mu\, \dot{u}_2(\mathbf{r}', E_{12}) + b_\mu\, \ddot{u}_2(\mathbf{r}', E_{12})$	$E_{22} = 0.0000$
	$a_\mu\, u_2(\mathbf{r}', E_{22}) + b_\mu\, u_2(\mathbf{r}', E_{32})$	$E_{32} = 0.9470$

TABLE V. Structure type and experimental lattice parameters a for the calculated materials.

	Structure type	a (Å)
SiC	zinc blende	4.340 [81]
Si	diamond	5.431 [82]
BN	zinc blende	3.615 [31]
MgO	rocksalt	4.211 [83]
CaO	diamond	4.810 [84]
LiF	rocksalt	4.010 [81]
Ar	fcc	5.260 [31]
C	diamond	3.567 [85]
GaAs	zinc blende	5.653 [86]

TABLE VI. Investigated materials together with the corresponding input parameters. The abbreviation $RG_{\max}$ stands for $R^{\mathrm{MT}} \cdot |\mathbf{G}+\mathbf{k}|_{\max}$. Calculations were performed on a $4 \times 4 \times 4$ **k** grid. In all binary materials but CaO, both atomic spheres have the same radii R^{MT}.

	$RG_{\max}$	R^{MT} (bohrs)	No. of empty states	No. of nl terms	MB size at Γ
SiC	11	1.6	350	46360	1460
Si	10	2.1	300	48828	1373
BN	11	1.4	350	53956	1315
MgO	11	1.6	350	54946	1443
CaO	11	2.0/1.8	350	43956	1383
LiF	11	1.6	450	45753	1275
Ar	11	2.75	350	60378	741
C	10	1.4	300	46360	1143
GaAs	11	2.2	350	42195	1779

For the integration over frequencies [Eq. (20)], we take into account 32 values, and $\omega_0 = 1$ Ha is chosen in the double Gaussian quadrature algorithm. For the nl terms in the self-energy matrix, we choose an energy threshold $\epsilon_{nl}^{\max}$; only states n and l with energies below $\epsilon_{nl}^{\max}$ build the upper triangle of the self-energy, leading to a number of nl terms (see Table VI). Based on our tests, disregarded higher-energy states have no effect on the final result (see Appendix C).

APPENDIX C: CONVERGENCE BEHAVIOR

We perform convergence tests with respect to (i) **k** grid, (ii) number of empty states, (iii) number of nl terms entering the self-energy, and $R^{\mathrm{MT}} \cdot |\mathbf{G}+\mathbf{k}|_{\max}$ ($RG_{\max}$) starting with MgO as the first example. In Fig. 11, the behavior with respect to the number of empty states is displayed for the parameter set used in production (green symbols). For this material, an extrapolation as employed by Refs. [59,73] turned out not adequate. To reach nevertheless convergence, calculations are carried out with reduced parameters [87] (blue symbols), including the first 150 unoccupied bands for the off-diagonal terms $R^{\mathrm{MT}} \cdot |\mathbf{G}+\mathbf{k}|_{\max} = 10$ and 20 frequencies, as summarized in Table VII. This allowed for including more empty states. We conclude that convergence is reached with 400 empty states and, thus, the result for the production settings (Table I) requires a correction of $+0.05$ eV, labeled Δ^{es} in Table VIII.

The convergence with respect to the number of off-diagonal terms shows an oscillatory behavior the production settings, as shown in Fig. 12. From the tests carried out with reduced parameters, we reach convergence already at 181 states which corresponds to roughly 60% of the whole energy spectrum. The same does not apply to the production settings, where the 88% of the whole energy spectrum is considered for the last data point and, yet, there is oscillating behavior. Aside from the case with no nl terms, the differences between the last two points are within 30 meV, as shown in Fig. 12.

To test the convergence with respect to $R^{\mathrm{MT}} \cdot |\mathbf{G}+\mathbf{k}|_{\max}$ ($RG_{\max}$), we again make use of the reduced settings (Table VII). As the calculations are converged at $RG_{\max} = 11$, and for the production settings a value of 12 was used, no correction is needed, i.e., $\Delta^{RK} = 0$.

Finally, we assess the quality of the **k** grid. From Table VIII we learn that we have to correct the results from the productions settings by $\Delta^{k} = -0.22$, i.e., the difference between the calculations with $6 \times 6 \times 6$ and $4 \times 4 \times 4$ grids, using the reduced parameters.

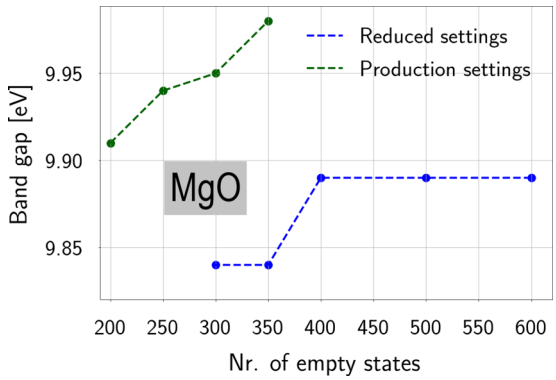

FIG. 11. Convergence of the fundamental band gap of MgO with respect to the number of empty states. The production settings are described in Appendix B, the reduced settings are summarized in Table VII.

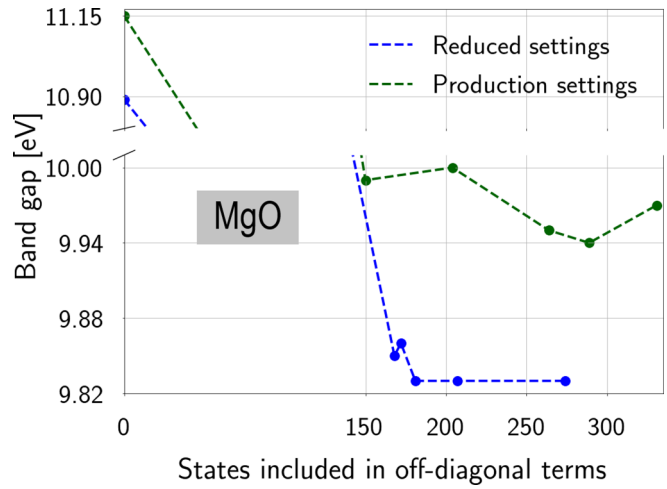

FIG. 12. Convergence of the fundamental band gap of MgO with respect to the number of nl terms.

TABLE VII. Reduced parameter settings used for convergence tests. For calculations probing convergence for LiF and Ar with respect to **k** grid, the numbers of local orbitals and *nl* terms are further reduced and their values are shown at the left in the corresponding columns.

	$RG_{\max}$	Number of empty states	Number of frequencies	Number of *nl* terms	Number of LOs
MgO	10	300	20	14028	13
LiF	10	300	20	21736/24753	9/74
Ar	12	350	16	21528/24753	8/61

For the case of Ar, the band gap converges to 15.34 eV at 350 empty states for the production setting, thus, there is no need for further correction in this regard. Likewise, convergence tests with respect to $R^{\mathrm{MT}} \cdot |\mathbf{G}+\mathbf{k}|_{\max}$ using a reduced set show a converged result already at a value of 11. The calculation of Ar is carried out including practically all states in the off-diagonal terms (leaving out only the last 15 of 355 states), therefore, no additional convergence was necessary.

In the calculation of LiF, the number of LOs is reduced to 74 (see Table VII) in order to account for up to 500 empty states. The fitted curve for this convergence curve reaches convergence at 500 empty states. The correction between 450 and 500 empty states corresponds to +0.02 eV. Likewise, for the off-diagonal terms, we find that using the reduced setting we reach convergence when including 277 empty states in the *nl* terms which amounts to 92% of the total empty states. For the production parameter set, this percentage corresponds to 414 out of a total of 450 empty states. The fitted curve for the results using reduced parameters returns a correction of −0.4 eV to the band gap when we take into account the 92% of empty states. Tests regarding $R^{\mathrm{MT}} \cdot |\mathbf{G}+\mathbf{k}|_{\max}$ include cases, showing convergence at a value of 10. Therefore, we conclude that also for this material there is no need for a correction due to the choice of $R^{\mathrm{MT}} \cdot |\mathbf{G}+\mathbf{k}|_{\max}$.

TABLE VIII. Band gap E_g (eV) at Γ for MgO, Ar, and LiF obtained for three **k** grids. Δ^k is the difference between the $4\times4\times4$ and $6\times6\times6$ **k** grids; Δ^{es} (Δ^{RK}) is a correction accounting for the number of empty states (basis-set size). Likewise, Δ^{nl} is a correction with respect to the number of *nl* terms. The last column shows the band gaps obtained by correcting the results from Table I by considering all the corrections.

	$2\times2\times2$	$4\times4\times4$	$6\times6\times6$	Δ^k	Δ^{nl}	Δ^{es}	Δ^{RK}	E_g^{corr}
MgO	9.71	9.86	9.64	−0.22	0	0.05	0	9.82
Ar	15.38	14.96	14.83	−0.13	0	0	0	15.21
LiF	16.70	16.61	16.47	−0.13	−0.04	0.02	0	16.46

[1] P. Hohenberg and W. Kohn, Phys. Rev. **136**, B864 (1964).
[2] W. Kohn and L. J. Sham, Phys. Rev. **137**, A1697 (1965).
[3] L. Hedin, Phys. Rev. **139**, A796 (1965).
[4] W. G. Aulbur, L. Jonsson, and J. W. Wilkins, Solid State Phys. **54**, 1 (2000).
[5] M. S. Hybertsen and S. G. Louie, Phys. Rev. B **34**, 5390 (1986).
[6] F. Aryasetiawan and O. Gunnarsson, Rep. Prog. Phys. **61**, 237 (1998).
[7] T. Körzdörfer and N. Marom, Phys. Rev. B **86**, 041110(R) (2012).
[8] G. Onida, L. Reining, R. W. Godby, R. Del Sole, and W. Andreoni, Phys. Rev. Lett. **75**, 818 (1995).
[9] F. Caruso, M. Dauth, M. J. van Setten, and P. Rinke, J. Chem. Theory Comput. **12**, 5076 (2016).
[10] F. Bruneval, J. Chem. Theory Comput. **15**, 4069 (2019).
[11] D. Golze, M. Dvorak, and P. Rinke, Front. Chem. **7**, 377 (2019).
[12] M. van Schilfgaarde, T. Kotani, and S. Faleev, Phys. Rev. Lett. **96**, 226402 (2006).
[13] S. V. Faleev, M. van Schilfgaarde, and T. Kotani, Phys. Rev. Lett. **93**, 126406 (2004).
[14] T. Kotani, M. van Schilfgaarde, and S. V. Faleev, Phys. Rev. B **76**, 165106 (2007).
[15] F. Aryasetiawan and O. Gunnarsson, Phys. Rev. B **49**, 16214 (1994).
[16] M. Betzinger, C. Friedrich, and S. Blügel, Phys. Rev. B **81**, 195117 (2010).
[17] H. Jiang, R. I. Gómez-Abal, X.-Z. Li, C. Meisenbichler, C. Ambrosch-Draxl, and M. Scheffler, Comput. Phys. Commun. **184**, 348 (2013).
[18] C. Draxl and M. Scheffler, J. Phys. Mater. **2**, 036001 (2019).
[19] S. Ismail-Beigi, J. Phys.: Condens. Matter **29**, 385501(2017).
[20] S. Ismail-Beigi, arXiv:1406.0772.
[21] S. Ismail-Beigi, Phys. Rev. B **81**, 195126 (2010).
[22] R. Del Sole, L. Reining, and R. W. Godby, Phys. Rev. B **49**, 8024 (1994).
[23] W. Chen and A. Pasquarello, Phys. Rev. B **92**, 041115(R) (2015).
[24] M. Shishkin, M. Marsman, and G. Kresse, Phys. Rev. Lett. **99**, 246403 (2007).
[25] D. R. Hamann and D. Vanderbilt, Phys. Rev. B **79**, 045109 (2009).
[26] I. Aguilera, C. Friedrich, and S. Blügel, Phys. Rev. B **91**, 125129 (2015).
[27] N. Marzari and D. Vanderbilt, Phys. Rev. B **56**, 12847 (1997).
[28] I. Souza, N. Marzari, and D. Vanderbilt, Phys. Rev. B **65**, 035109 (2001).
[29] J. I. Mustafa, S. Coh, M. L. Cohen, and S. G. Louie, Phys. Rev. B **92**, 165134 (2015).
[30] S. Tillack, A. Gulans, and C. Draxl, Phys. Rev. B **101**, 235102 (2020).
[31] M. Shishkin and G. Kresse, Phys. Rev. B **75**, 235102 (2007).
[32] F. Bruneval, N. Vast, and L. Reining, Phys. Rev. B **74**, 045102 (2006).
[33] M. van Schilfgaarde, T. Kotani, and S. V. Faleev, Phys. Rev. B **74**, 245125 (2006).
[34] P. YU and M. Cardona, *Fundamentals of Semiconductors*, 4th ed. (Springer, Berlin, 2010).

[35] B. Monserrat and R. J. Needs, Phys. Rev. B **89**, 214304 (2014).
[36] C. Kittel, *Introduction to Solid State Physics*, 6th ed. (Wiley, New York, 1986).
[37] N. Izyumskaya, D. O. Demchenko, S. Das, Ü. Özgür, V. Avrutin, and H. Morkoç, Adv. Electron. Mater. **3**, 1600485 (2017).
[38] G. Antonius, S. Poncé, E. Lantagne-Hurtubise, G. Auclair, X. Gonze, and M. Côté, Phys. Rev. B **92**, 085137 (2015).
[39] R. Whited, C. J. Flaten, and W. Walker, Solid State Commun. **13**, 1903 (1973).
[40] M. Piacentini, D. W. Lynch, and C. G. Olson, Phys. Rev. B **13**, 5530 (1976).
[41] M. Cardona, Solid State Commun. **133**, 3 (2005).
[42] L. Ley, R. A. Pollak, F. R. McFeely, S. P. Kowalczyk, and D. A. Shirley, Phys. Rev. B **9**, 600 (1974).
[43] A. Svane, N. E. Christensen, I. Gorczyca, M. van Schilfgaarde, A. N. Chantis, and T. Kotani, Phys. Rev. B **82**, 115102 (2010).
[44] A. N. Chantis, M. van Schilfgaarde, and T. Kotani, Phys. Rev. Lett. **96**, 086405 (2006).
[45] D. Deguchi, K. Sato, H. Kino, and T. Kotani, Jpn. J. Appl. Phys. **55**, 051201 (2016).
[46] B. Monserrat, G. J. Conduit, and R. J. Needs, Phys. Rev. B **90**, 184302 (2014).
[47] G. Antonius, S. Poncé, P. Boulanger, M. Côté, and X. Gonze, Phys. Rev. Lett. **112**, 215501 (2014).
[48] F. Bechstedt, K. Seino, P. H. Hahn, and W. G. Schmidt, Phys. Rev. B **72**, 245114 (2005).
[49] S. Botti and M. A. L. Marques, Phys. Rev. Lett. **110**, 226404 (2013).
[50] D. Åberg, B. Sadigh, and P. Erhart, Phys. Rev. B **85**, 125134 (2012).
[51] F. Kaplan, M. E. Harding, C. Seiler, F. Weigend, F. Evers, and M. J. van Setten, J. Chem. Theory Comput. **12**, 2528 (2016).
[52] Cohen Aron J., Mori-Sánchez Paula, and Yang Weitao, Chem. Rev. **112**, 289 (2012).
[53] C. Draxl, D. Nabok, and K. Hannewald, Acc. Chem. Res. **47**, 3225 (2014).
[54] M. Bolorizadeh, V. Sashin, A. Kheifets, and M. Ford, J. Electron Spectrosc. Relat. Phenom. **141**, 27 (2004).
[55] A. Yamasaki and T. Fujiwara, Phys. Rev. B **66**, 245108 (2002).
[56] G. Vidal-Valat, J. P. Vidal, and K. Kurki-Suonio, Acta Crystallogr., Sect. A **34**, 594 (1978).
[57] V. A. Sashin, H. E. Dorsett, M. A. Bolorizadeh, and M. J. Ford, J. Chem. Phys. **113**, 8175 (2000).
[58] P. Liao and E. A. Carter, Phys. Chem. Chem. Phys. **13**, 15189 (2011).
[59] R. Rodrigues Pela, U. Werner, D. Nabok, and C. Draxl, Phys. Rev. B **94**, 235141 (2016).
[60] R. Pela (private communication).
[61] P. Koval, D. Foerster, and D. Sánchez-Portal, Phys. Rev. B **89**, 155417 (2014).
[62] S. Das, J. E. Coulter, and E. Manousakis, Phys. Rev. B **91**, 115105 (2015).
[63] J. E. Coulter, E. Manousakis, and A. Gali, Phys. Rev. B **88**, 041107(R) (2013).
[64] A. Stoyanova, A. O. Mitrushchenkov, L. Hozoi, H. Stoll, and P. Fulde, Phys. Rev. B **89**, 235121 (2014).
[65] Y.-N. Xu and W. Y. Ching, Phys. Rev. B **44**, 7787 (1991).
[66] I. Aguilera, C. Friedrich, G. Bihlmayer, and S. Blügel, Phys. Rev. B **88**, 045206 (2013).
[67] J. C. Slater, Phys. Rev. **51**, 846 (1937).
[68] D. J. Singh, *Planewaves, Pseudopotentials, and the LAPW Method*, 2nd ed. (Springer, New York, 2006).
[69] O. K. Andersen, Phys. Rev. B **12**, 3060 (1975).
[70] D. Singh, Phys. Rev. B **43**, 6388 (1991).
[71] C. Ambrosch-Draxl, Phys. Scr. **2004**, 48 (2004).
[72] E. Sjöstedt, L. Nordström, and D. J. Singh, Solid State Commun. **114**, 15 (2000).
[73] D. Nabok, A. Gulans, and C. Draxl, Phys. Rev. B **94**, 035118 (2016).
[74] T. Kotani and M. van Schilfgaarde, Solid State Commun. **121**, 461 (2002).
[75] C. Friedrich, A. Schindlmayr, and S. Blügel, Comput. Phys. Commun. **180**, 347 (2009).
[76] A. Gulans, S. Kontur, C. Meisenbichler, D. Nabok, P. Pavone, S. Rigamonti, S. Sagmeister, U. Werner, and C. Draxl, J. Phys.: Condens. Matter **26**, 363202 (2014).
[77] C. Ambrosch-Draxl and J. O. Sofo, Comput. Phys. Commun. **175**, 1 (2006).
[78] H. J. Vidberg and J. W. Serene, J. Low Temp. Phys. **29**, 179 (1977).
[79] S. Lebègue, B. Arnaud, M. Alouani, and P. E. Bloechl, Phys. Rev. B **67**, 155208 (2003).
[80] O. Andersen, Solid State Commun. **13**, 133 (1973).
[81] V. N. Staroverov, G. E. Scuseria, J. Tao, and J. P. Perdew, Phys. Rev. B **69**, 075102 (2004).
[82] C. R. Hubbard, H. E. Swanson, and F. A. Mauer, J. Appl. Crystallogr. **8**, 45 (1975).
[83] A. Grüneis, G. Kresse, Y. Hinuma, and F. Oba, Phys. Rev. Lett. **112**, 096401 (2014).
[84] P. Richet, H.-K. Mao, and P. M. Bell, J. Geophys. Res. Solid Earth **93**, 15279 (1988).
[85] T. Hom, W. Kiszenik, and B. Post, J. Appl. Crystallogr. **8**, 457 (1975).
[86] A. S. Cooper, Acta Crystallogr. **15**, 578 (1962).
[87] C. Friedrich, M. C. Müller, and S. Blügel, Phys. Rev. B **83**, 081101(R) (2011).